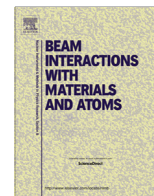




Contents lists available at ScienceDirect

## Nuclear Instruments and Methods in Physics Research B

journal homepage: [www.elsevier.com/locate/nimb](http://www.elsevier.com/locate/nimb)

## Dynamic defect annealing in wurtzite MgZnO implanted with Ar ions

A.Yu. Azarov<sup>a,\*</sup>, E. Wendler<sup>b</sup>, X.L. Du<sup>c</sup>, A.Yu. Kuznetsov<sup>a</sup>, B.G. Svensson<sup>a</sup><sup>a</sup> University of Oslo, Department of Physics, Centre for Materials Science and Nanotechnology, PO Box 1048 Blindern, N-0316 Oslo, Norway<sup>b</sup> Friedrich-Schiller-Universität Jena, Institut für Festkörperphysik, Max-Wien-Platz 1, 07743 Jena, Germany<sup>c</sup> Institute of Physics, The Chinese Academy of Sciences, Beijing 100190, China

## ARTICLE INFO

## Article history:

Received 25 February 2015

Received in revised form 9 May 2015

Accepted 9 May 2015

## Keywords:

ZnO

MgZnO

Radiation defects

Ion implantation

## ABSTRACT

Successful implementation of ion beams for modification of ternary ZnO-based oxides requires understanding and control of radiation-induced defects. Here, we study structural disorder in wurtzite ZnO and Mg<sub>x</sub>Zn<sub>1-x</sub>O ( $x \leq 0.3$ ) samples implanted at room and 15 K temperatures with Ar ions in a wide fluence range ( $5 \times 10^{12}$ – $3 \times 10^{16}$  cm<sup>-2</sup>). The samples were characterized by Rutherford backscattering/channeling spectrometry performed *in-situ* without changing the sample temperature. The results show that all the samples exhibit high radiation resistance and cannot be rendered amorphous even for high ion fluences. Increasing the Mg content leads to some damage enhancement near the surface region; however, irrespective of the Mg content, the fluence dependence of bulk damage in the samples displays the so-called IV-stage evolution with a reverse temperature effect for high ion fluences.

© 2015 Elsevier B.V. All rights reserved.

## 1. Introduction

ZnO is wide and direct band gap semiconductor ( $E_g = 3.4$  eV) which has received tremendous research interest during the past decade because of its numerous promising applications in optoelectronics for the UV range [1,2]. Band gap modulation is essential for the realization of heterostructures and it has been shown that alloying of ZnO with MgO ( $E_g = 7.8$  eV) enables an increase of  $E_g$  up to 4.5 eV and still keeping the wurtzite structure [3,4]. Despite that ion implantation has a number of advantages over other doping techniques, energetic particles produce defects affecting almost all materials properties. Understanding and control of implantation-induced defects are crucial for a successful utilization of ion beams in device processing.

Even for pure ZnO the mechanisms of defect formation during ion implantation and subsequent annealing are still not well understood despite large efforts in the past decade [5–9]. In particular, the origin of the high radiation resistance of ZnO, commonly associated to efficient dynamic defect annealing even at cryogenic temperatures [5,6], is not clear. Further, it has been demonstrated that the surface termination affects the radiation tolerance of wurtzite ZnO and samples with non-polar surface terminations exhibit higher radiation resistance as compared to c-plane terminated ones [7]. However, despite that ZnO is generally not amorphized even at high fluences of heavy ions, strong dopant-defect

reactions can retard the dynamic annealing resulting in disorder enhancement and eventually amorphization, as has been demonstrated for Si [5] and B [8] ions. A compelling evidence of the important role of the implanted species on the thermal stability of radiation damage in ZnO can also be found in [9]. Hence, in the present contribution we have used noble Ar ions in order to eliminate such dopant-related effects on the damage evolution. However, it should be noted that for high Ar fluences processes related to Ar bubble formation may affect the defect formation.

The incorporation of a third element in a binary compound can also dramatically affect the mechanisms of ion-induced damage formation. For instance, it has been shown that an increase in Al content strongly enhances dynamic annealing in AlGaAs [10] and AlGaN [11], and also that a small amount of Al or In in GaN dramatically suppresses the commonly observed preferential surface disordering in pure GaN [11]. In contrast, our previous studies have shown that an increase in Mg content has a weak effect on the disorder accumulation in wurtzite MgZnO implanted at room temperature (RT) and primarily affects disordering near the surface [12]. In this work, we present a comparative analysis of damage formation in wurtzite Mg<sub>x</sub>Zn<sub>1-x</sub>O ( $x \leq 0.3$ ) and ZnO implanted at RT and 15 K with Ar<sup>+</sup> ions over a wide range of fluences ( $5 \times 10^{12}$ – $3 \times 10^{16}$  cm<sup>-2</sup>). Thermally-activated dynamic annealing processes are expected to be suppressed to a large extent at 15 K and a comparison of the disorder formation with that at RT provides a possibility to elucidate the fundamental mechanisms involved in the defect formation.

\* Corresponding author.

E-mail address: [aazarov@smn.uio.no](mailto:aazarov@smn.uio.no) (A.Yu. Azarov).

## 2. Experimental

Approximately 1  $\mu\text{m}$  thick wurtzite  $\text{Mg}_x\text{Zn}_{1-x}\text{O}$  ( $x = 0.1$  and  $0.3$ ) layers were grown by molecular beam epitaxy (MBE) on  $c$ -oriented sapphire substrate (the details of the growth process can be found elsewhere [13]). The samples were implanted with 160 keV  $\text{Ar}^+$  ions at low temperature (15 K) and RT in a fluence range of  $5 \times 10^{12}$ – $3 \times 10^{16}$   $\text{cm}^{-2}$ . The ion flux was kept at  $3 \times 10^{11}$   $\text{cm}^{-2} \text{s}^{-1}$  for low fluences and was increased up to  $6 \times 10^{12}$   $\text{cm}^{-2} \text{s}^{-1}$  for the highest fluence used. Note that the flux was kept the same for the samples implanted with the same fluences irrespective of the implantation temperature. According to TRIM code [14] simulations, the projected range ( $R_p$ ) of 160 keV  $\text{Ar}$  ions and the

maximum of the nuclear energy loss profile ( $R_{pd}$ ) are estimated to be  $\sim 105$  and  $\sim 65$  nm, respectively, in  $\text{Mg}_x\text{Zn}_{1-x}\text{O}$  ( $x = 0.1$  and  $0.3$ ). In the simulations we have used a  $\text{Mg}_x\text{Zn}_{1-x}\text{O}$  density obtained by linear interpolation between the densities of  $\text{ZnO}$  ( $5.6 \text{ g/cm}^3$ ) and  $\text{MgO}$  ( $3.58 \text{ g/cm}^3$ ). In addition, hydrothermally grown  $\text{ZnO}$  single crystals were implanted under the same conditions with 200 keV  $\text{Ar}^+$  ions and used as reference; here, the calculated values of  $R_p$  and  $R_{pd}$  are  $\sim 135$  and  $\sim 75$  nm, respectively. All the implants were carried out at  $11^\circ$  off the  $[0001]$  direction in order to minimize channeling.

The structural quality of the implanted samples was analyzed by Rutherford backscattering spectrometry in channeling mode (RBS/C) with 1.4 MeV  $^4\text{He}^+$  ions incident along the  $[0001]$

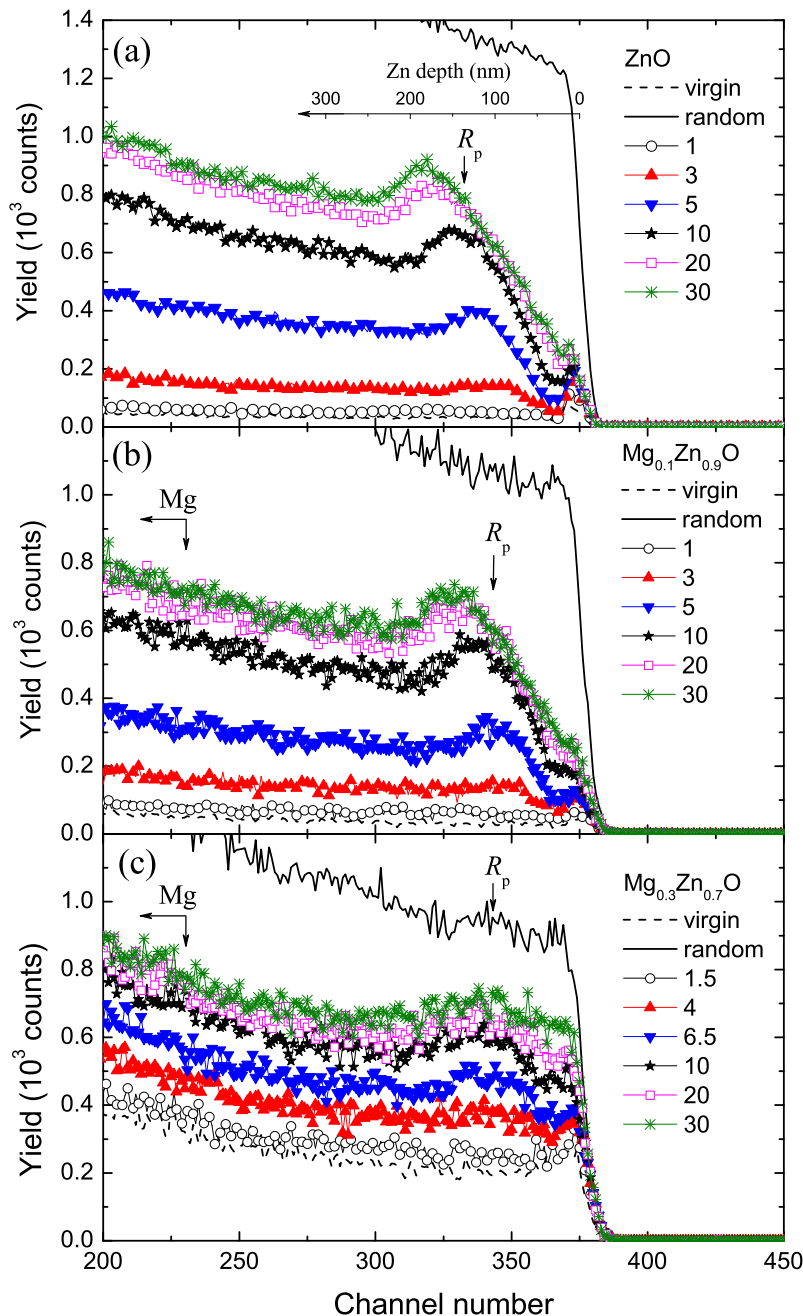


**Fig. 1.** RBS/C spectra of (a)  $\text{ZnO}$  (b)  $\text{Mg}_{0.1}\text{Zn}_{0.9}\text{O}$  and (c)  $\text{Mg}_{0.3}\text{Zn}_{0.7}\text{O}$  implanted at 15 K with  $\text{Ar}^+$  ions to different fluences as indicated in the legend (in  $10^{15}$   $\text{at/cm}^2$ ). The projected ranges ( $R_p$ ) of the implanted ions in correlation with the Zn depth scale and Mg surface position are shown by the arrows. The channeling spectra of virgin samples are also depicted for comparison by the dashed lines.

direction and backscattered into a detector at  $170^\circ$  relative to the incident beam direction. The RBS/C spectra were acquired *in-situ* without changing the sample temperature after implantation (the details of the experimental set-up can be found in [15]). Analysis of the raw RBS/C spectra was performed using the DICADA code [16] to deduce an effective number of scattering centers under the assumption of randomly displaced lattice atoms representing point defects, defect clusters or amorphous zones. The calculated number of scattering centers normalized to the atomic concentration is referred to below as “relative disorder”. Because of the large difference in atomic mass between Zn and O(Mg) and the relatively low Mg content in the samples investigated, we limit our analysis to the damage on the Zn-sublattice only. Uncertainties in the determination of the relative disorder are of statistical origin and highest for the lowest fluences ( $\sim 25\%$ ) with a decrease to 5% for the highest fluence.

### 3. Results and discussion

Fig. 1 illustrates the damage buildup in (a) ZnO, (b)  $\text{Mg}_{0.1}\text{Zn}_{0.9}\text{O}$  and (c)  $\text{Mg}_{0.3}\text{Zn}_{0.7}\text{O}$  samples implanted at 15 K to Ar fluences at and above  $10^{15} \text{ cm}^{-2}$ . Even at the highest fluence used ( $3 \times 10^{16} \text{ cm}^{-2}$ ) the backscattering yield in channeling direction does not reach the random level. This means that amorphization does not occur indicating strong dynamic annealing also at cryogenic temperatures irrespective of the Mg content. Furthermore, all the spectra are characterized by a very high dechanneling background and a relatively low contribution of direct backscattering. This points to the existence of extended defects such as dislocation loops and/or

stacking faults [17,18], which do not contribute to direct backscattering of the analyzing ions.

Despite that ZnO and  $\text{Mg}_{0.1}\text{Zn}_{0.9}\text{O}$  exhibit similar damage accumulation with a well defined peak in the crystal bulk, the accumulation in  $\text{Mg}_{0.3}\text{Zn}_{0.7}\text{O}$  is enhanced in the near surface region. In fact, the general trends of the damage buildup in the  $\text{Mg}_{0.3}\text{Zn}_{0.7}\text{O}$  samples – saturation as a function of ion fluence, enhanced disorder level near the surface and enhanced height of the dechanneling yield behind the damage peak – are similar to those observed in  $\text{Mg}_{0.3}\text{Zn}_{0.7}\text{O}$  samples implanted with heavy ions [12]. It should be noted that the as-grown  $\text{Mg}_{0.3}\text{Zn}_{0.7}\text{O}$  samples exhibit a quite high minimum yield ( $\chi_{\text{min}}$ ) of  $\sim 20\%$  in contrast to that in the ZnO and  $\text{Mg}_{0.1}\text{Zn}_{0.9}\text{O}$  samples where  $\chi_{\text{min}}$  does not exceed 3.5% indicating a good crystalline quality of these samples. Such a high value of  $\chi_{\text{min}}$  in the  $\text{Mg}_{0.3}\text{Zn}_{0.7}\text{O}$  samples suggests the presence of defects already in the as-grown state. These defects can act either as nucleation sites for the ion-induced damage build-up or as sinks for generated point defects and, hence, affect the damage accumulation, specifically in the low fluence regime when the damage starts to nucleate.

The evolution of bulk damage growth in MgZnO implanted at 15 K is illustrated by Fig. 2 showing (a) the maximum relative disorder in the bulk damage peaks and (b) their positions as a function of ion fluence. Independently on the Mg content, the bulk disorder exhibits a IV-stage behavior with two fast growing stages (I and III) and two saturation ones (stages II and IV). Interestingly, the Mg content does not affect the defect saturation levels corresponding to  $\sim 0.02$  and  $\sim 0.6$  for the stages II and IV, respectively. Note that, the tendency of a higher damage formation at low fluences as well as a less abrupt stage III in the  $\text{Mg}_{0.3}\text{Zn}_{0.7}\text{O}$  samples, compared to

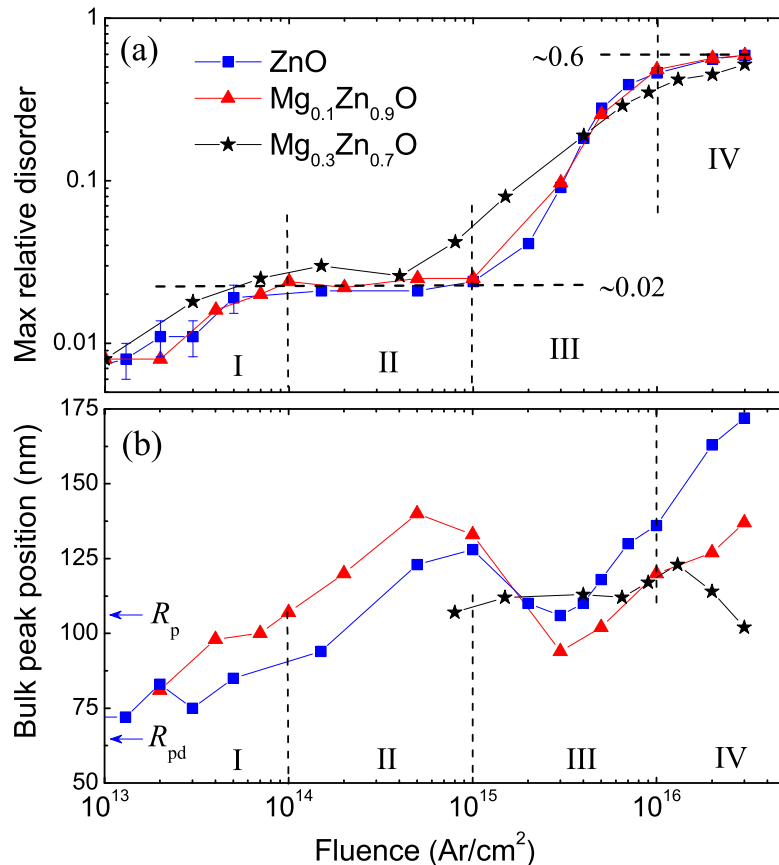


Fig. 2. (a) Maximum relative disorder on the Zn-sublattice in the bulk damage peaks of  $\text{Mg}_x\text{Zn}_{1-x}\text{O}$  samples implanted at 15 K and (b) their positions as a function of Ar fluence. The vertical dashed lines separate the different damage accumulation stages indicated by Roman numbers (see the text for details). The values of  $R_p$  and  $R_{pd}$  for MgZnO are shown by the arrows in the panel (b). Error bars are shown in the panel (a) for the low fluences only where the uncertainty is largest.

those for the other samples, can be attributed to their poorer initial crystalline quality, as discussed above. For the ZnO and  $\text{Mg}_{0.1}\text{Zn}_{0.9}\text{O}$  samples, the bulk damage peak occurs initially close to  $R_{pd}$  but with increasing fluence at stages I and II the damaged layer extends further into the bulk with an apparent shift of the peak maximum position well beyond  $R_p$ . Stage III is characterized by a rapidly growing damage peak amplitude starting at a depth between  $R_{pd}$  and  $R_p$ . The peak consists now of two (at least) contributions with a new one emerging around  $R_p$  and which becomes dominant at fluences in the mid  $10^{15} \text{ cm}^{-2}$  range. This leads to an apparent decrease in the damage peak position towards  $R_p$  (see Fig. 2(b)), before it moves deeper again for high fluences in stage III and stage IV. The rapidly growing contribution around  $R_p$  is most likely associated with the high content of implanted Ar ions promoting defect nucleation/accumulation. Further, despite that the damage level exhibits saturation in stage IV the profile expands both into the bulk and towards the sample surface with increasing fluence and a similar expansion holds for the high fluences at stage III. However, the expansion towards the surface is less efficient in the ZnO and  $\text{Mg}_{0.1}\text{Zn}_{0.9}\text{O}$  samples leading to an apparent shift of the damage peak position to higher depths with increasing fluence. This evolution is attributed to defect migration and annihilation at the sample surface which acts as an efficient sink for point defects mobile at cryogenic temperatures.

Interestingly a similar mechanism has been put forward to explain a fluence dependent shift of a bulk damage peak in GaN [23]. Evidently, this process requires that the effective diffusion length of the mobile point defects is comparable to or higher than the distance between the defect generation region and the sample surface.

Note that, the position of the damage peak in the  $\text{Mg}_{0.3}\text{Zn}_{0.7}\text{O}$  samples is not possible to resolve clearly, especially at low fluences due to the broad damage profiles without a well defined peak position. This broad damage profile can be attributed to an enhanced accumulation of disorder near the surface and/or the high dechanneling yield in the un-implanted  $\text{Mg}_{0.3}\text{Zn}_{0.7}\text{O}$  samples compared to that in the  $\text{Mg}_{0.1}\text{Zn}_{0.9}\text{O}$  and ZnO samples. However, for high fluences, the damage peak position in  $\text{Mg}_{0.3}\text{Zn}_{0.7}\text{O}$  is essentially independent on the ion fluence (Fig. 2(b)) and corresponds well to  $R_p$  indicating less efficient dynamic defect annealing at the surface with increasing Mg content.

It should be noted that there are striking similarities between the bulk damage evolution observed in the present wurtzite ZnO(MgZnO) samples and that found in other non-amorphizable II–VI materials with high degree of dynamic annealing at low temperatures, such as CdTe [19], as well as in SiC [20] at elevated irradiation temperature where dynamic annealing is expected to be efficient. Possible mechanisms of defect formation at each stage

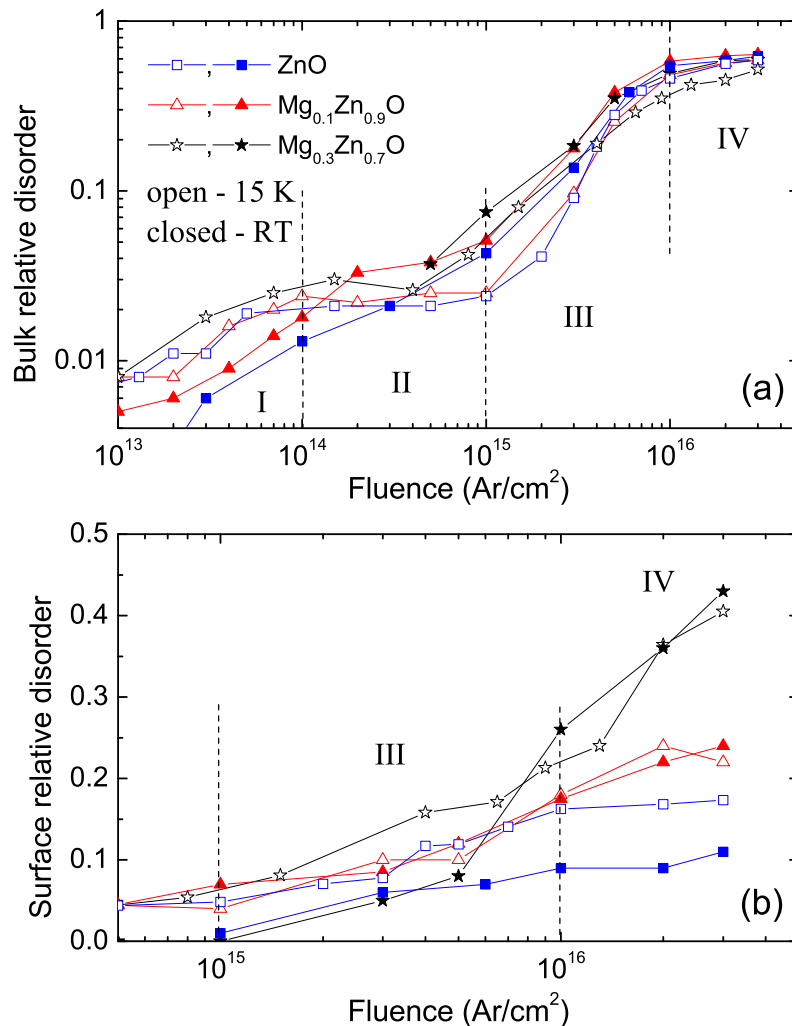


**Fig. 3.** Fluence dependence of the maximum relative disorder on the Zn-sublattice in (a) the bulk damage peak region and (b) at the surface of  $\text{Mg}_x\text{Zn}_{1-x}\text{O}$  ( $x = 0, 0.1$  and  $0.3$ ) samples implanted at 15 K (open symbols) and RT (closed symbols). The vertical dashed lines separate the different damage accumulation stages indicated by Roman numbers (see the text for details).

was discussed in [19,21]; for example, the stages I and III correspond to the formation of point defects/point-defect complexes and more stable larger defect clusters/extended defects, respectively. More recently it has also been demonstrated that the implanted species can play a crucial role on the disorder formation/stabilization at stage III [8]. Moreover, implantation-induced strain can also affect the damage stabilization at stage III as well as the transition between the stages III and IV, as demonstrated in [22].

Fig. 3 shows the fluence dependence of the maximum relative disorder at (a) the bulk damage peak and (b) the surface after implantation at RT and 15 K. Irrespective of the Mg content, all the samples exhibit similar trends with temperature. In the low fluence regime (stage I) a higher damage level occurs for the 15 K implantation, while the opposite holds for high fluences (stages III and IV). A disorder enhancement with decreasing temperature is anticipated and usually attributed to the suppression of dynamic annealing; such a dependence is commonly observed in most semiconductors including GaN [24,25] for temperatures at and below RT and SiC [20,26]. The mechanisms responsible for the opposite trend at the stages III and IV are more intriguing. In Ref. [8], we have suggested that such a reverse temperature effect on the disorder accumulation may be due to a decreasing mobility of the generated point defects, which have to migrate some distance before being trapped by stable defect structures. According to the results in Fig. 2(b), this distance has to be on the order of 30–50 nm. A similar reverse temperature effect on the damage accumulation has also been observed in high fluence implanted yttria-stabilized zirconia single crystals [27], and it was attributed to an enhanced defect clustering (on the expense of defect annihilation) because of an increase in defect mobility with increasing temperature. For GaN implanted at elevated temperatures, somewhat contradictory results exist in the literature; for instance, Wenzel et al. [28] reported an enhanced damage accumulation in Mg implanted samples when increasing the implantation temperature from RT to 823 K. In contrast, Kucheyev et al. [29] observed a normal damage behavior for Au ions in the same temperature range. In its turn, Usov et al. [30] observed a reverse behavior for Ar implantation but in a rather narrow temperature range of 773–973 K. A possible explanation of the different results may be the implanted species and their role for defect stabilization at elevated temperatures, and this holds also for Ar at high fluences where thermally activated Ar clustering and/or bubble formation can be anticipated [31].

According to Figs. 1(a) and 3(b), the surface disorder is weak in ZnO with some enhancement at 15 K compared to that at RT which can be attributed to less efficient defect annihilation at low temperature. However, Fig. 3(b) also demonstrates that increasing Mg content leads to enhanced surface disorder with negligible temperature dependence up to RT. At elevated temperatures, a growing surface disorder in MgZnO samples has been reported, and for example, it has been shown that surface decomposition/erosion leading to dramatic compositional and phase changes take place in heavily damaged MgZnO films at ~1000 K [32]. However, the processes causing the growth in surface disorder for the MgZnO samples in Fig. 3(b) appear to be ballistic in nature and promoted by the Mg content.

#### 4. Conclusions

An increasing Mg content leads to damage enhancement in the near surface region, but the evolution of bulk damage in wurtzite MgZnO at 15 K exhibits an “ordinary” IV-stage behavior with ion fluence, similar to that found in pure ZnO and other II–VI and III–V materials with a high degree of dynamic defect annealing. The

low fluence regime (stage I) displays “normal” behavior with an enhanced disorder at low temperature relative to RT, while for high ion fluences (stages III and IV) the damage formation shows a reverse temperature effect. In contrast to the bulk damage, the variation of implantation temperature has only a minor effect on the accumulation of surface disorder, except for the pure ZnO samples where an “ordinary” dependence is found.

#### Acknowledgements

This work was performed within The Norwegian Research Centre for Solar Cell Technology (project number 460976), a Centre for Environment-friendly Energy Research cosponsored by the Norwegian Research Council and research and industry partners in Norway.

#### References

- [1] Ü. Özgür, Ya.I. Alivov, C. Liu, A. Teke, M.A. Reshchikov, S. Doğan, V. Avrutin, S.-J. Cho, H. Morkoç, *J. Appl. Phys.* 98 (2005) 041301.
- [2] Y.W. Heo, D.P. Norton, L.C. Tien, Y. Kwon, B.S. Kang, F. Ren, S.J. Pearton, J.R. LaRoche, *Mat. Sci. Eng. R* 47 (2004) 1.
- [3] T. Makino, Y. Segawa, M. Kawasaki, A. Ohtomo, R. Shiroki, K. Tamura, T. Yasuda, H. Koinuma, *Appl. Phys. Lett.* 78 (2001) 1237.
- [4] X. Du, Z. Mei, Z. Liu, Y. Guo, T. Zhang, Y. Hou, Z. Zhang, Q. Xue, A.Yu. Kuznetsov, *Adv. Mater.* 21 (2009) 4625.
- [5] S.O. Kucheyev, J.S. Williams, C. Jagadish, J. Zou, C. Evans, A.J. Nelson, A.V. Hamza, *Phys. Rev. B* 67 (2003) 094115.
- [6] K. Lorenz, E. Alves, E. Wendler, O. Bilani, W. Wesch, M. Hayes, *Appl. Phys. Lett.* 87 (2005) 191904.
- [7] S. Charnvanichborikarn, M.T. Myers, L. Shao, S.O. Kucheyev, *J. Appl. Phys.* 114 (2013) 213512.
- [8] A.Yu. Azarov, E. Wendler, A.Yu. Kuznetsov, B.G. Svensson, *Appl. Phys. Lett.* 104 (2014) 052101.
- [9] A.Yu. Azarov, A. Hallén, P. Rauwel, X.L. Du, A.Yu. Kuznetsov, B.G. Svensson, *J. Appl. Phys.* 115 (2014) 073512.
- [10] H.H. Tan, C. Jagadish, J.S. Williams, J. Zou, D.J.H. Cockayne, A. Sikorski, *J. Appl. Phys.* 77 (1995) 87.
- [11] S.O. Kucheyev, J.S. Williams, J. Zou, C. Jagadish, *J. Appl. Phys.* 95 (2004) 3048.
- [12] A.Yu. Azarov, B.G. Svensson, A. Hallén, X.L. Du, A.Yu. Kuznetsov, *J. Appl. Phys.* 108 (2010) 033509.
- [13] Z.L. Liu, Z.X. Mei, T.C. Zhang, Y.P. Liu, Y. Guo, X.L. Du, A. Hallén, J.J. Zhu, A.Yu. Kuznetsov, *J. Cryst. Growth* 311 (2009) 4356.
- [14] J.F. Ziegler, J.P. Biersack, U. Littmark, *The Stopping and Range of Ions in Solids*, vol. 1, Pergamon, New York, 1985, pp. 109. <www.srim.org>.
- [15] B. Breeger, E. Wendler, W. Trippensee, Ch. Schubert, W. Wesch, *Nucl. Instrum. Methods Phys. Res. B* 174 (2001) 661.
- [16] K. Gärtner, *Nucl. Instrum. Methods Phys. Res. B* 227 (2005) 522.
- [17] E. Wendler, O. Bilani, K. Gärtner, W. Wesch, M. Hayes, F.D. Auret, K. Lorenz, E. Alves, *Nucl. Instrum. Methods Phys. Res. B* 267 (2009) 2708.
- [18] A. Turos, L. Nowicki, A. Stonert, K. Pagowska, J. Jagielski, A. Muecklich, *Nucl. Instrum. Methods Phys. Res. B* 268 (2010) 1718.
- [19] C.W. Rischau, C.S. Schnohr, E. Wendler, W. Wesch, *J. Appl. Phys.* 109 (2011) 113531.
- [20] E. Wendler, Th. Bierschenk, W. Wesch, E. Friedland, J.B. Malherbe, *Nucl. Instrum. Methods Phys. Res. B* 268 (2010) 2996.
- [21] W. Wesch, E. Wendler, C.S. Schnohr, *Nucl. Instrum. Methods Phys. Res. B* 277 (2012) 58.
- [22] A. Turos, P. Jozwik, L. Nowicki, N. Sathish, *Nucl. Instrum. Methods Phys. Res. B* 332 (2014) 50.
- [23] A.I. Titov, P.A. Karaseov, A.Yu. Kataev, A.Yu. Azarov, S.O. Kucheyev, *Nucl. Instrum. Methods Phys. Res. B* 277 (2012) 80.
- [24] S.O. Kucheyev, J.S. Williams, C. Jagadish, J. Zou, G. Li, *Phys. Rev. B* 62 (2000) 7510.
- [25] E. Wendler, W. Wesch, A.Yu. Azarov, N. Catarino, A. Redondo-Cubero, E. Alves, K. Lorenz, *Nucl. Instrum. Methods Phys. Res. B* 307 (2013) 394.
- [26] A.Yu. Kuznetsov, J. Wong-Leung, A. Hallén, C. Jagadish, B.G. Svensson, *J. Appl. Phys.* 94 (2003) 7112.
- [27] A. Debelle, J. Channagiri, L. Thomé, B. Décamps, A. Boule, S. Moll, F. Garrido, M. Behar, J. Jagielski, *J. Appl. Phys.* 115 (2014) 183504.
- [28] A. Wenzel, C. Liu, B. Rauschenbach, *Mater. Sci. Eng. B* 59 (1999) 191.
- [29] S.O. Kucheyev, J.S. Williams, J. Zou, C. Jagadish, G. Li, *Nucl. Instrum. Methods Phys. Res. B* 178 (2001) 209.
- [30] I. Usov, N. Parikh, D.B. Thomson, R.F. Davis, *MRS Internet J. Nitride Semicond. Res.* 7 (2002) 9.
- [31] C. Silva, A.R.G. Costa, M.M. Cruz, R.C. da Silva, R.P. Borges, L.C. Alves, M. Godinho, *J. Phys.: Condens. Matter* 22 (2010) 346005.
- [32] A.Yu. Azarov, A. Hallén, X.L. Du, Z.L. Liu, B.G. Svensson, A.Yu. Kuznetsov, *Phys. Rev. B* 84 (2011) 014114.